The Astrophysical Journal, 714:644–651, 2010 May 1 doi:10.1088/0004-637X/714/1/644

STREAMER WAVES DRIVEN BY CORONAL MASS EJECTIONS

Y. Chen, H. Q. Song, B. Li, L. D. Xia, Z. Wu, H. Fu, and Xing Li[1]
Shandong Provincial Key Laboratory of Optical Astronomy and Solar-Terrestrial Environment, School of Space Science and Physics, Shandong University at Weihai, Weihai 264209, China; yaochen@sdu.edu.cn
Received 2009 December 31; accepted 2010 March 18; published 2010 April 13

ABSTRACT

Between 2004 July 5 and July 7, two intriguing fast coronal mass ejection (CME)–streamer interaction events were recorded by the Large Angle and Spectrometric Coronagraph. At the beginning of the events, the streamer was pushed aside from its equilibrium position upon the impact of the rapidly outgoing and expanding ejecta; then, the streamer structure, mainly the bright streamer belt, exhibited elegant large-scale sinusoidal wavelike motions. The motions were apparently driven by the restoring magnetic forces resulting from the CME impingement, suggestive of magnetohydrodynamic kink mode propagating outward along the plasma sheet of the streamer. The mode is supported collectively by the streamer-plasma sheet structure and is therefore named "streamer wave" in the present study. With the white light coronagraph data, we show that the streamer wave has a period of about 1 hr, a wavelength varying from 2 to 4 solar radii, an amplitude of about a few tens of solar radii, and a propagating phase speed in the range 300–500 km s^{-1}. We also find that there is a tendency for the phase speed to decline with increasing heliocentric distance. These observations provide good examples of large-scale wave phenomena carried by coronal structures and have significance in developing seismological techniques for diagnosing plasma and magnetic parameters in the outer corona.

Key words: waves – magnetohydrodynamics (MHD) – Sun: corona – Sun: coronal mass ejections (CMEs)

1. INTRODUCTION

Wave phenomena represent the most fundamental and straightforward response of a system with plasmas and magnetic fields to perturbations arising from either interior or exterior. The solar atmosphere, serving as a good example, is very dynamic by nature on all relevant temporal-spatial scales, and is therefore expected to be able to support various wave modes with different observational manifestations. Indeed, with the development of observational techniques, many types of wave or wavelike phenomena have been discovered in the solar atmosphere. For instance, compressible density perturbations moving outward are detected inside coronal plumes (Ofman et al. 1997, 1999; DeForest & Gurman 1998), propagating longitudinal waves are found in coronal loops (Berghmans & Clette 1999), and many other phenomena driven by nearby solar eruptions, including coronal loop oscillations (Aschwanden et al. 1999; Nakariakov et al. 1999), coronal shocks (Sime & Hundhausen 1987; Sheeley et al. 2000), and the so-called Moreton (Moreton & Ramsey 1960) and EIT waves (Thompson et al. 1998; Wills-Davey & Thompson 1999), are observed. Extensive observational and theoretical studies have been conducted to investigate the nature of these dynamical phenomena (e.g., Aschwanden 2004; Nakariakov & Verwichte 2005; Ofman 2009; and references therein). These studies, generally speaking, provide valuable information on the coronal medium through which the waves propagate.

Helmet streamers are the most conspicuous large-scale quasi-steady structures extending from the lower to outer corona. In the white light images observed by a coronagraph, a well-developed streamer is delineated by a sharp brightness boundary. The boundary separates the streamer from its surroundings. Besides the boundary, a typical streamer also includes a bunch of closed field arcades, a streamer cusp, and a high-density plasma sheet (also called the streamer stalk or streamer belt) within which a long thin current sheet is embedded (see, e.g, Pneuman & Kopp 1971; Suess & Nerney 2006). On the other hand, coronal mass ejections (CMEs), representing the largest and most energetic dynamical process in the corona, may cause global perturbations with a timescale of minutes to hours. Therefore, close interactions between CMEs and streamers can frequently occur, especially during the active phase of a solar cycle when CMEs and streamers are present at virtually all heliolatitudes. In general, CME–streamer-relevant events can be classified into two groups. One comprises those events of CMEs originating and erupting from the streamer interior, like the so-called streamer blowouts (Howard et al. 1985; Hundhausen 1993) or streamer puffs (Bemporad et al. 2005). On the other hand, the events in the second group result from the streamers being hit on the sides by either CMEs with expanding structures or by CME-driven disturbances like shock waves. The collision may cause apparent deflections or kinks of streamer rays tracing the passage of CME disturbances (Sheeley et al. 2000). In some cases, the collision may have triggered reconnections across the streamer current sheet as indicated by the observed streamer disconnection (e.g., Bemporad et al. 2008), the release of plasma blobs along the streamer stalk, or the formation of streamer in/out pairs (e.g., Sheeley & Wang 2007).

Given the fundamental role played by wave excitations in a disturbed plasma-magnetic field system, one natural question arises—can the streamer respond in the form of observable waves or wavelike motions to a strong impact from a CME ejecta? If yes, what modes are they? In the following text, an answer to the above questions will be provided with two observational examples of streamer wavy motions driven by CMEs. Their overall details as revealed from the white-light coronagraph data will be described in Section 2. In Section 3, we present our data manipulation method to extract the profile of the wavy motion and give the resultant physical analysis of one of the two events in Section 4. In Section 5, we discuss briefly the CME–streamer sources and the other

[1] On sabbatical leave from Institute of Mathematics and Physics, Aberystwyth University, UK, SY23 3BZ.

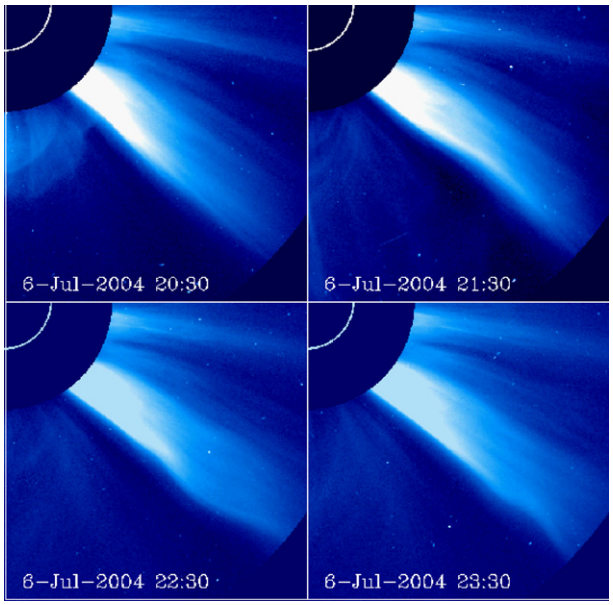

Figure 1. Wavelike motion of a streamer stalk observed by LASCO C2 on 2004 July 6, as an aftermath of the CME impact. Only the southwest quadrants of the full FOV of the LASCO C2 observations taken at 20:30, 21:30, 22:30, and 23:30 are shown. The static images at other moments, relevant RDIs, and animations of the whole process can be conveniently viewed from the online CDAW CME database.

observational event. The final section presents our conclusions and discussion.

2. LASCO DATA: WHITE LIGHT AND RUNNING DIFFERENCE IMAGES

From 2004 July 3 to July 7, the Large Angle and Spectrometric Coronagraph (LASCO) on the *Solar and Heliospheric Observatory (SOHO)* observed a well-defined bright streamer in the southwest quadrant with a position angle of about 231°. The dynamical behavior of this streamer structure serves as the main subject of this study. In this interval of streamer observation, a total of 16 CME eruptions with various sizes and sources are recorded by LASCO according to the online CDAW (Coordinated Data Analysis Workshops) CME catalog. Two of these events are relevant to our study, which were first observed by LASCO C2 at 23:06 UT on July 5 and 20:06 UT on July 6, respectively. Both events are classified as fast full-halo BA (Brightness-Asymmetric) CMEs (check the CDAW web for details of CME classifications, and many other information), both appear to be brighter in the southern heliosphere, and both seem to originate from the back side of the Sun as indicated by the absence of eruptive features on the front side. The linear speeds of the two eruptions are 1444 and 1307 km s^{-1}, according to the CDAW catalog. From the online CDAW animations of the two CMEs, one can see that both eruptions produce visible impact on the streamer dynamics. At the beginning of the events,

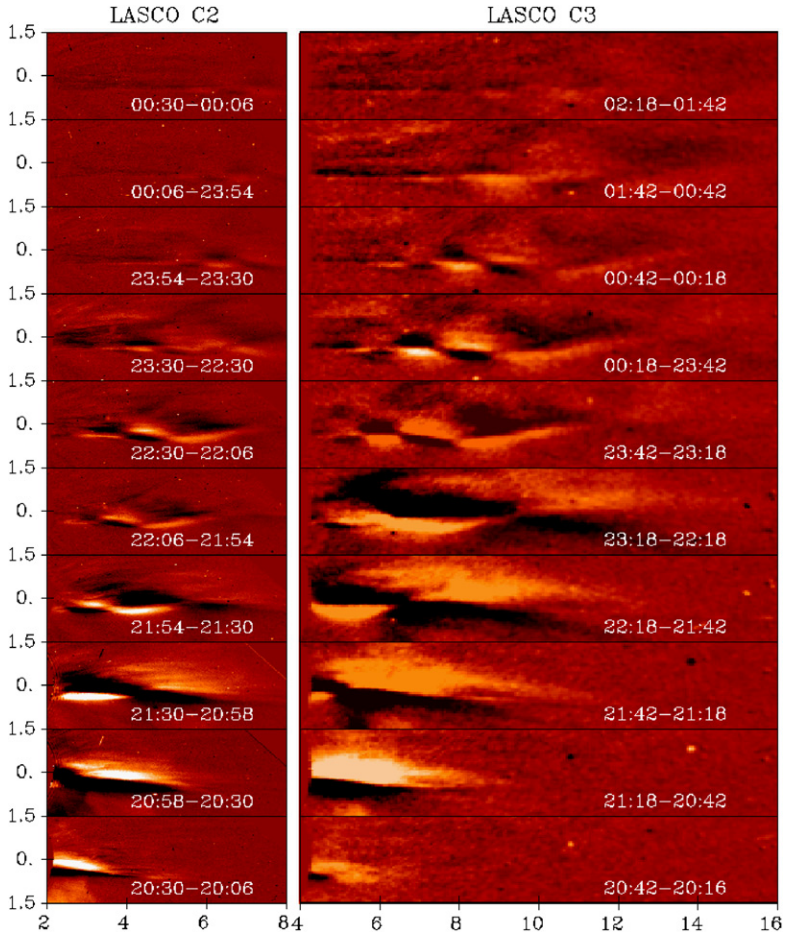

Figure 2. Two stacks of strips scissored from the corresponding rotated RDIs from LASCO C2 (left) and C3 (right). The difference times are given in the figure. The two vertical sides of the strips are both 1.5 $R_\odot$ away from the Sun, and the two horizontal sides are 2(4) and 8(16) $R_\odot$ away from the Sun for C2(C3)'s observations. See the text for more details.

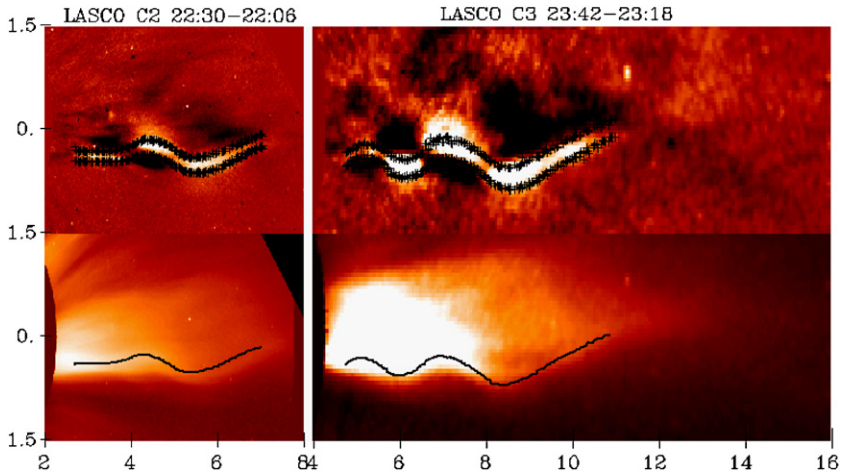

Figure 3. Examples demonstrating the method used to extract wave profiles from the RDIs obtained by LASCO C2 (left) and C3 (right) observations. The two curves given by plus signs in the upper panels are obtained by six times of delineating the upper and lower boundaries of the bright patches. The algebraic average of the two sets of measurements gives the single curve plotted in the lower panels.

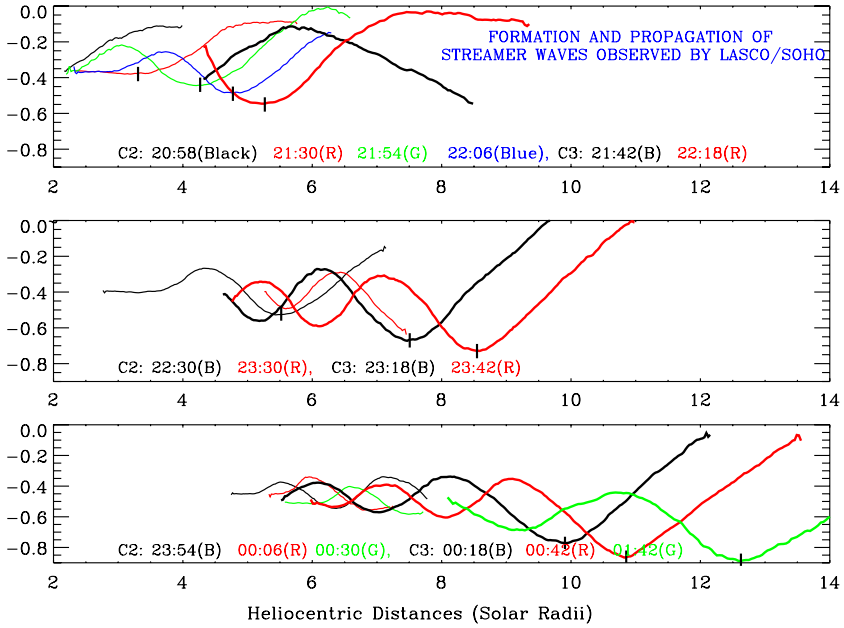

Figure 4. Streamer wave profiles at various instants extracted from the rotated RDI strips with the approach presented in the third section. The profiles from the C2 (thin curves) and C3 (thick curves) observations are colored and assembled into three panels according to the observational times which are given at the bottom of each panel and colored correspondingly. The short vertical lines represent the positions of phase P1 at various wave profiles. The vertical and horizontal scales are both in units of solar radii.

the streamers were pushed aside from their initial equilibrium position upon the impact of the rapidly outgoing and expanding ejecta; then, the streamer structure, mainly the bright streamer belt, exhibited apparent large-scale sinusoidal (or snake-like) wavy motions. The wavy motions of the streamer are the phenomena we put our focus on in the present study. In the latter event, starting late on July 6, the wavy feature is much more obvious. Therefore, in what follows we first conduct a detailed analysis of this latter event and then provide a brief discussion of the earlier one.

To illustrate the overall process of the wavelike motion of the streamer, in Figure 1 we present four white-light images for the southwest quadrant of the full field of view (FOV) of the LASCO C2 observations taken at 20:30, 21:30, 22:30, and 23:30. The inner white circle represents the size of the Sun, and the black plate gives the inner occulting disk of LASCO C2. The FOV is from 2 $R_\odot$ to 7.8 $R_\odot$ for the southwest corner with the concerned streamer. The CME front enters the C2 FOV at 20:06, as mentioned. From Figure 1, we see that at 20:30, the CME front is still in the FOV, which pushes the streamer aside from its equilibrium position. By 21:30, the CME front has already left the FOV due to the large outgoing speed of about 1300 km s^{-1}. Comparing the streamer features at the same heights in the upper two images, we see that the position where the streamer is strongly deflected gets higher following the CME ejecta, and the lower part of the streamer starts to bounce back. In the lower two panels, a sinusoidal motion is clearly seen to propagate outward along the streamer stalk. The motion is also evident from the online animation provided by the CDAW database. To conduct a more quantitative analysis of the streamer motion, we need to delineate the wave profiles from the coronagraph observations. However, it proves difficult to work directly with the white light images like those shown in Figure 1, as a result of the inhomogeneous mass distribution

of the streamer structure and the interference of the bright features above the streamer, especially when the wave amplitude gets smaller with increasing time and height. Therefore, we examine the running difference images (RDIs for short) instead, looking for an alternative approach of plotting the wave profiles. The RDIs, obtained by subtracting a previous image from the current one, are extensively used in image manipulations of solar observations to highlight the region of brightness change between subsequent exposures.

In Figure 2, we show two stacks of strips scissored from the corresponding RDIs from LASCO C2 (left) and C3 (right). The difference times are given in the figure. To get this figure, we first rotate each RDI counterclockwise by 39° to put the streamer horizontally. Then, we pick out a long strip containing the streamer. The two vertical sides of the strip are both 1.5 $R_\odot$ away from the Sun, and the two horizontal sides are 2(4) and 8(16) $R_\odot$ away from the Sun for C2(C3)'s observations. From these RDIs, we note that most of the bright features above the streamer that obscure the wave profile now disappear, and the wavy motions of the streamer, even in the latter stage of the event when the wave amplitude gets smaller, are better recognizable. The most prominent feature in the stack of RDI strips of Figure 2 is given by the interesting bright-dark and dark-bright pairs. From the definition of image difference, the presence of such pairs is caused by the displacements of high-density streamer features from bright to dark regions. Therefore, they are a straightforward manifestation of the propagating snakelike motion we have observed in the white light images.

Now, we take a closer examination of the temporal series of RDI strips in Figure 2. The bottom three strips, one from C2 and two from C3, show large areas of bright-upper and dark-lower (BD for short) regions indicating the deflection of the streamer body by the CME ejection. In the following two ones (C2: 20:58-20:30, C3: 21:42-21:18), a region of opposite pattern with the color distribution being dark-upper and bright-lower (DB for short) emerges from the inner part of the corresponding FOV. This is a clear indication that the streamer starts to bounce backward from the deflection. The DB pattern moves outward to about 4.2 and 6.2 $R_\odot$ in the FOV of C2 at 21:30 and C3 at 22:18, respectively. In the strips at 21:54-21:30 for C2 and 23:18-22:18 for C3, the BD pattern re-emerges indicating the streamer moves again in the same direction as pushed by the CME, a result of the overshoot of the streamer bouncing motion. The change of color pattern from BD to DB, or vice versa, is continuously observed till the brightness difference is too weak to discern. In total, two to three DB-BD pairs are detected, indicating that there are two to three observable periods of the streamer wavy perturbation. From C2 observations, we see that between 20:55 and 21:54 the streamer accomplishes the first period of wavy motion, and before 22:30, another half period is present. From C3, we see that between 23:42 and 21:42, two periods of the streamer wavy motion, i.e., two DB-BD pairs, are formed. We therefore deduce that the period of the motion is approximately 1 hr. We also realize that we are actually fortunate to have most inter-exposure intervals close to one-half of the period, i.e., one-half hour. As a result of this coincidence, at a fixed location a wave crest may be replaced by a wave trough in the subsequent exposure. This makes the RDIs very suitable for recognizing the propagating sinusoidal perturbation. There are three RDIs with inter-exposure intervals being one hour, 23:30-22:30 for C2, and 23:18-22:18 and 01:42-00:42 for C3. It can be seen that the pair of DB-BD features are not as clear as in the rest.

In the above analysis, we deduce that the period of the streamer wavy motion is about 1 hr as read from the upward and downward streamer displacements at the bottom of the LASCO FOV. Apparently, the restoring force supporting this motion is provided by the magnetic field of the streamer structure, which comes into play after the streamer deviates from its equilibrium position upon the CME impingement. The bouncing motion of the streamer further excites the outward-propagating sinusoidal perturbations. The energy received from the initial CME impact is then carried outward by the perturbations. Consequently, the bouncing amplitude of the streamer declines rapidly as observed. The perturbations are mostly propagating magnetohydrodynamic (MHD) wave excited by the bouncing motion of the lower part of the streamer, which is tentatively regarded as the kink mode collectively supported by the slab configuration of the streamer plasma sheet (Roberts 1981; Edwin & Roberts 1982). More discussion on the nature of the wave mode will be provided in the final section of this paper. In the following sections, we shall call these outward propagating perturbations streamer waves and conduct a more quantitative analysis of their properties.

3. METHOD TO EXTRACT THE WAVE PROFILE

In this section, we demonstrate the method used to extract the wave profile from RDIs. In general, each RDI contains the information of two consecutive white light observations, with bright regions representing where the streamer is at the posterior instant of the difference, and dark regions giving where the streamer was at the preceding moment. However, the bright or dark regions usually are distributed discretely as shown in Figure 2. Therefore, one needs to make subjective judgements regarding the wave trends when linking those bright or dark patches together as a whole, and it is always necessary for one to keep an eye on the associated white light images to correctly determine the wave profile. In other words, the deduced wave profile must be consistent with the wavy motion observed from white light images. In the following section, the method used to extract the wave profile is demonstrated using the RDI strips at 22:30-22:08 for C2 and 23:42-23:18 for C3 which are shown again in Figure 3 in larger versions. The inter-exposure intervals are both 24 minutes, close to half of the wave period obtained previously; therefore, both RDIs present well-recognized brightness distribution patterns with DB-BD pairs.

In Figure 3, the two curves given by plus signs in the upper panels are obtained by six times of delineating and linking the upper and lower boundaries of the bright patches, which are employed to represent the wave profiles. The algebraic average of the two sets of measurements gives the single line plotted in the lower panels where the white light images at 22:30 for C2 and 23:42 for C3 are also shown. We see that the wave profile obtained from boundary delineation in RDIs is basically consistent with the wavy motion revealed in the white light images. However, the obtained RDI wave profile does not strictly follow the white light brightness boundary. The reason is threefold. First, the bright and dark regions in RDIs indicate the locations where the brightness or the plasma density changes significantly, while the brightness boundary in the white light images just reflect the outer border of the streamer structure. Second, the streamer wave studied here is supported collectively by the streamer structure, which spreads over a finite range vertically across the streamer stalk. This range is mainly determined by the width of the streamer part that is waving, and is apparently different at different heights. Third, the plasmas

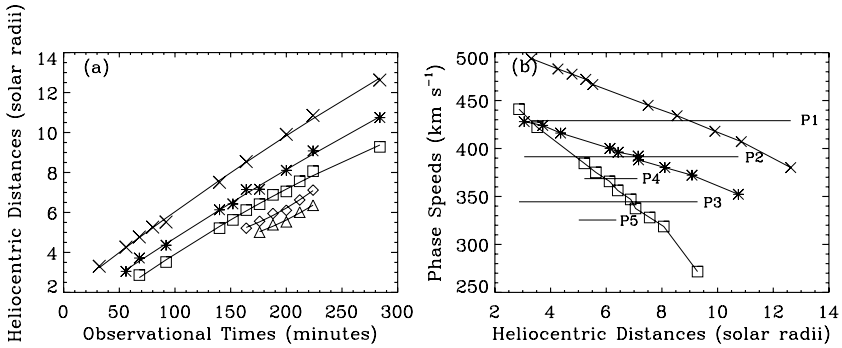

Figure 5. (a) Heliocentric distances of the five specific phases P1–P5, represented by crosses, asterisks, squares, diamonds, and triangles, respectively. The solid lines are given by a second-order polynomial fitting to the relevant distance-time profiles. The horizontal axis is given by the observational times starting from 20:58 UT. (b) Variation of the linear phase speeds for P1–P5 with heliocentric distances (horizontal solid lines), and the phase speeds for P1 (crosses), P2 (asterisks), and P3 (squares) given by the distance-time polynomial fitting. The relative uncertainties of the phase distances are estimated to be about ±10% of the local wavelength and that of the phase speeds about ±10% of the plotted values.

are distributed very non-uniformly across the streamer structure, so plasmas at different locations may have different weights in supporting the wavy motion.

As mentioned, there are three RDIs in Figure 2 whose difference intervals are as large as the wave period; therefore, it is not straightforward to extract the wave profile from these RDIs. For the RDIs at 23:30-22:30 for C2 and 23:18-22:18 for C3, to yield the wave profile at the present moment (i.e., 23:30 for C2 and 23:18 for C3) we simply delineate and link the boundary of the dark patches in the corresponding subsequent RDI, which has an appropriate exposure interval of 24 minutes. Since the brightness difference is too weak to be useful at the RDI of 02:18-01:42, we still delineate and link the bright patches in RDI of 01:42-00:42. This gives the last wave profile to be shown in Figure 4.

4. STREAMER WAVE ANALYSIS

Figure 4 shows a collection of streamer wave profiles at various instants extracted from the rotated RDI strips with the approach presented in the previous section. The profiles from the C2 (thin curves) and C3 (thick curves) observations are colored and assembled into three panels according to the observational times which are given at the bottom of each panel and colored correspondingly. The vertical and horizontal scales are both in units of solar radii. This figure unambiguously confirms the presence of the streamer wavy motion. The reader can compare any two consecutive wave profiles with the associated RDI or the white light images to verify the deduced profiles. With Figure 4, we are able to conveniently conduct quantitative measurements of wave properties like the wavelength, the perturbation amplitude, and the propagation phase speed.

Before doing this, let us first describe some general features as manifested by the wave profiles. It can be seen that at 20:58, the downward displacement of the streamer reaches maximum at the bottom of C2's FOV; this produces a wave trough, which marks the initiation of the investigated streamer wave. From 20:58 to 21:54, nearly 1 hr apart, the streamer moves upward and then downward to form a complete wavelength with two wave troughs and a wave crest. The wave phase associated with the first trough is referred to as phase one or P1 for short. Similarly, the following crest, the second trough, the second crest, and the third trough are referred to as P2, P3, P4, and P5, respectively. The heliocentric distances of these five specified wave phases will be measured to evaluate the propagation phase speeds.

In Figure 4, the positions of P1 at various wave profiles, when present, are indicated by black vertical lines. The positions of other wave phases can be easily read from the associated profiles. It can be seen that at 22:18, P1 is located at about 5.2 $R_\odot$, which is replaced by the following wave trough P3 one hour later at 23:18, in agreement with the previous assessment of the wave period. Similar rough yet consistent estimates can be carried out using the rest of the wave profiles, for example, using the anti-correlated red and black thick lines in the lower two panels.

It is also easy to confirm that there presents two complete wavelengths spanning from P1 to P5. Hereafter, we refer to the profile from P1 to P3, i.e., the first wavelength, as W1, and the profile from P3 to P5 as W2. As seen from the delineated wave profiles, the complete W1 becomes observable after 21:54 by C2 and 23:18 by C3, and the complete W2 becomes observable after 23:54 for C2 and 00:18 next day for C3. Both the amplitude and wavelength of W1 get larger during propagation, while the data for W2 are not sufficient for one to draw similar conclusions. It is also found that within the same range of heliocentric distances, the wavelength and amplitude of W2 are smaller than their counterparts of W1. For example, the W1 wavelength (amplitude) at 23:18 or 23:42 is about 2.5 (0.5) $R_\odot$ larger than the W2 wavelength of 1.7 (0.2) $R_\odot$ at 00:42 within the same range of 6–8 $R_\odot$. The temporal increase of the W1 amplitude may be attributed to the tendency for the energy flux density to be conserved during propagation. The decrease of the amplitude from W1 to W2 is not due to a local damping mechanism of the wave energy. Instead, it is a result of the convection of the source energy with the outward propagation of the wave. The factor accounting for the wavelength change will be further discussed based on the following measurements of the phase speeds.

Now, we shall focus on the deduction of propagation phase speeds by measuring and fitting the heliocentric distances of the five specified phases P1–P5. The obtained distances are shown in Figure 5(a), where the crosses, asterisks, squares, diamonds, and triangles represent the distances of P1–P5. The solid lines are given by a second-order polynomial fitting to the relevant distance-time profiles. The horizontal axis of this figure represents the observational times starting from 20:58 UT. The increase of the W1 wavelength with time is clearly illustrated by the increase of distance between P1 and P3 lines. The average phase speeds for P1–P5 are 429, 391, 344, 369, and 325 km s^{-1}, respectively, which are shown as the five horizontal solid lines in Figure 5(b), where the heliocentric distances

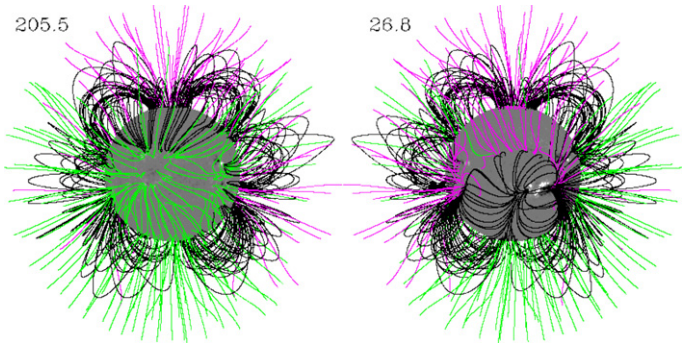

Figure 6. Coronal magnetic field topologies obtained from the SSW PFSS model, with central longitudes being 205.°5 (left) and 26.°8 (corresponding to the Carrington times of 2004 July 6 20:00 and July 20 08:00). The closed field lines are colored black, and the open outward (inward) field lines are represented with purple (green) lines.

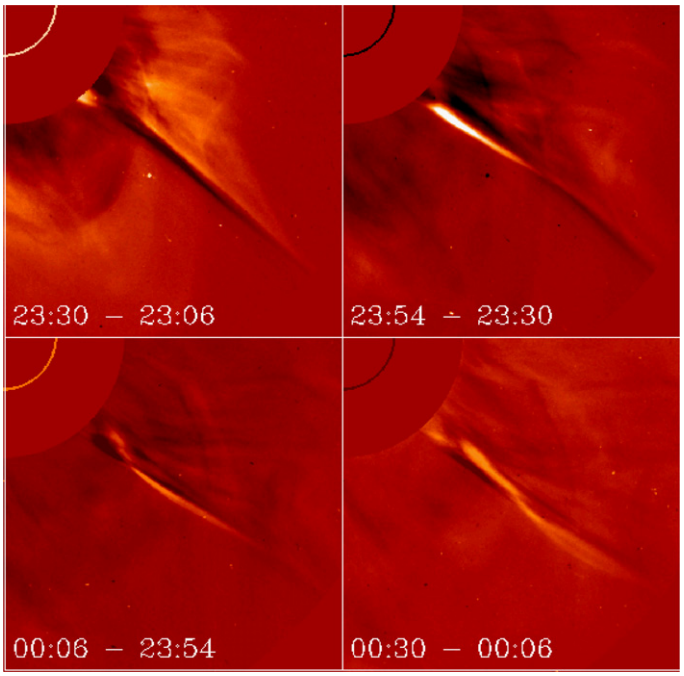

Figure 7. Four RDIs of the southwest quadrant of the FOV of LASCO C2 for the CME–streamer wave event observed on July 5.

are used as the abscissa. For P1–P3, we also show the phase speeds derived by the second-order polynomial fitting plotted in Figure 5(a). The fitted speeds for P4 and P5 are not shown since the accuracy of the polynomial fitting is greatly reduced by the small number of available distance measurements.

From the values of the average phase speeds, we see that the average speed of the preceding phase is faster than that of the trailing phase, except that P4 moves slightly faster than P3 by about 25 km s^{-1}. Such a difference of phase speeds is possibly less than the uncertainties of our measurements, and therefore not significant. A rough estimate on the uncertainties and relevant impacts on our conclusions will be given in the following paragraph. From the fitted velocity profiles of P1–P3, we see that there exists a general trend for the phase speed to decrease with increasing distance, and again, preceding phases move faster than trailing ones. If we assume that the period keeps basically constant during the wave propagation, then the wavelength is mainly determined by the phase speeds. Thus, the variations of the phase speeds shown in Figure 5(b) can provide explanations for the previously mentioned wavelength changes of W1 and from W1 to W2. To be specific, the result that the difference between the phase speeds of P1 and P3 gets larger with distance explains the wavelength increase of W1. The general larger propagation speed of W1 than that of W2 explains the positive difference between the two wavelengths. The large speed variations among various phases at a fixed location are possibly due to the disturbed state of the coronal plasmas and magnetic field topologies in the aftermath of the CME eruption.

Now, we proceed to give a rough estimate on the uncertainties of our measurements on the wavelength and the phase speed. There are two factors contributing to the errors of our measurements. One stems from the method we are using to delineate the wave profiles, and the other is from the determination of the distances of various phase points in the wave profiles. In the study, the wave profiles are algebraic averages of two sets of measurements obtained by delineating and linking the upper and lower boundaries of the bright (or dark) patches in RDIs. The uncertainties of determining the wave profiles including the locations of the crests and troughs should be no larger than one-third to a half of the length of the considered patch, which is about $\pm 10\%$ (or a total of 20%) of a local wavelength. Once the wave profiles are plotted, the contribution of the determination of phase point distances to the total error is not important, as proved by our practice of determining the phase point distances repeatedly for several times. The above error to the measurement of the wave profiles is passed directly to the calculation of the wavelength and phase speed. Therefore, the errors of the wavelength and phase speeds given by Figure 5 are estimated to be about $\pm 10\%$ of the presented values. We see that the phase speed differences between P3, P4, and P5 are smaller than or close to the relevant errors, and thus not significant. However, other conclusions deduced above remain unaffected in general.

The last issue that needs to be addressed in this section is related to the wave period determined from the above analysis. The period is about 1 hr, and the intervals of the LASCO C2 or C3's observations are both approximately 30 minutes. Thus, the data are sampled at roughly the Nyquist rate. This raises the issue of possible aliasing and incorrect determination of the period if the actual oscillation period is shorter than 30 minutes (for example, 20 minutes). The issue is addressed from the following two aspects of argument. First, the concerned imaging areas of the two LASCO coronagraphs are overlapping between 4 and 8 $R_\odot$, and the combination of the two sets of observations results in an effective exposure interval of 12 minutes mostly, as read from the exposure instants listed in Figures 2 and 4. Second, for an oscillation period as small as, say, 30 minutes, the average phase speed is 965 km s^{-1} with a wavelength of 2.5 $R_\odot$. As will be discussed in the discussion section of this paper, this means an Alfvén speed in the slow wind surrounding the plasma sheet significantly faster than that estimated from previous relevant theoretical calculations (e.g., Wang et al. 1998; Suess et al. 1999; Chen & Hu 2001, 2002; Hu et al. 2003; Li et al. 2006). According to these calculations, the plasma β should be no less than 0.1 in the slow wind regime surrounding the plasma sheet above the streamer cusp; this yields an Alfvén speed less than 575 km s^{-1} assuming an isothermal temperature of 1 MK for both electrons and protons. Therefore, we conclude that the value of the deduced wave period is unlikely to be affected by the aliasing issue raised above.

5. POSSIBLE CME SOURCES AND THE EARLIER EVENT OF STREAMER WAVE

As mentioned at the start of Section 2, the CME eruption that drives the streamer wavy motion seems to originate from the back side of the Sun. To provide more information on the magnetic topology of the CME source and the associated streamer, in Figure 6 we show two images of the coronal magnetic fields calculated using the photospheric fields for Carrington Rotation (CR) 2018 with the Solar Software (SSW) package PFSS (Potential Field Source Surface, Schatten et al. 1969). The central meridians of the two images are taken to be the Carrington longitudes of 205.°5 (left) and 26.°8 (right), corresponding to the Carrington times of 2004 July 06 20:00 and July 20 08:00. The closed field lines are colored black, and the open outward (inward) field lines are represented with purple (green) lines. Assuming that the global magnetic topology does not change significantly during the CR, we can regard the left image as the front side one and the right as the back side one at the time of the relevant CME occurrence. We see that the most probable CME source region is the active region group in the southeastern quadrant of the back side. This is consistent with the brightness asymmetric feature of the eruption. The concerned streamer is also mainly rooted in the back side, which nominally connects with the suggested CME source region through a highly inclined loop system. This configuration allows the CME ejecta to hit directly on the streamer stalk from the flank without causing any observable disruption of the streamer.

An earlier CME, first present in the C2 FOV at 23:06 UT on July 5, is also observed to drive apparent streamer wavy motions. The overall process of this earlier streamer wave event is presented in Figure 7 by four RDIs, where the familiar DB-BD features are observed. The deflection and bouncing of the streamer is evident from the first and the second images. The third image indicates that the streamer waves backward in the direction of the CME deflection, and the streamer bounces again to the opposite direction in the last image. It is seen that only one complete wavelength of the streamer wave is observable. And the streamer wave feature is not as clear as the one discussed in detail. A preliminary evaluation shows that the wave period is also about 1 hr; the wave amplitude, the wavelength, and the propagation phase speed are about 0.2 $R_\odot$, 2–4 $R_\odot$, and 400 km s^{-1}, respectively.

6. CONCLUSIONS AND DISCUSSION

In this paper, we conduct an observational study on the phenomena of streamer wave, which is excited by the CME impact and represents one of the largest wave phenomena ever discovered in the corona. The wave is mostly MHD kink mode propagating outward along the thin plasma sheet. The restoring force supporting the wavy motion is provided by the magnetic field of the streamer structure, which is generated by the large streamer deflection upon the CME impact. The energy received from the impact is carried outward by the wave perturbation. Consequently, the amplitude of the wave near the Sun declines rapidly with time, and only a few periods of the wave are observable. The wave period is estimated to be about 1 hr, the wavelength varies from 2 to 4 $R_\odot$, the wave amplitude is a few tens of solar radii, and the phase speed is about 300–500 km s^{-1}. There exists a general trend for the phase speed to decrease with increasing heliocentric distance.

Interactions between CME and streamers are frequently observed, especially during the active phase of solar cycles. Usually, such interactions result in apparent deflections of interacting streamers (e.g., Hundhausen et al. 1987; Sime & Hundhausen 1987; Sheeley et al. 2000). We emphasize that the streamer wavy motion, reported in the present study, is a direct consequence of a streamer deflection. Nevertheless, as revealed from a preliminary overview of the long-term LASCO observations, in only a very small fraction of the deflection events does the streamer exhibit wavelike phenomena. In other words, most CME-driven deflections, even very fast and strong, are not followed by a streamer wavy motion. Therefore, there exist certain strict conditions for streamer waves to be excited by a CME–streamer deflection. Two observational features of the July 6 event can help us evaluate the relevant conditions. First, it is found that the CME source region lies on the flank side of the closed loops comprising the streamer; that means the CME does not originate from beneath the streamer structure, and the ejecta can collide with the streamer from the flank side. Second, the CME is a fast eruption with a speed of $\geqslant$1300 km s^{-1}, which has two consequences favoring the excitation of the streamer wave. One is that a faster eruption results in a stronger impingement on the nearby streamer and a consequent larger deflection of the streamer structure from its equilibrium position; the other is that the ejecta moves out of the corona in a relatively short time and leaves enough time for the streamer wave to develop. Otherwise, if the eruption is not fast enough, the deflected streamer may simply move backward along with the ejecta, and no wavy motions result. To observe one example of such a case, one may check the online LASCO observations of the interaction event between a CME and a streamer in the northeastern quadrant dated on 2004 July 9. Sheeley et al. (2000) also present LASCO examples of strong streamer deflection events without accompanying apparent streamer wavy motions. It should be noted that a more complete understanding of the excitation conditions of the streamer wave can only be obtained from observational investigations on many more similar events and from elaborate theoretical modeling endeavors.

As mentioned in the introduction section, a well-developed typical streamer consists of the main body, which is a bunch of closed field arcades confining high-density coronal plasmas, and a dense plasma sheet within which a long thin current sheet is embedded. The intersection of the closed streamer main body and the open plasma sheet gives the streamer cusp, which is generally thought to be below 2–2.5 $R_\odot$, very close to the bottom of the LASCO C2 FOV. After the impact from a CME, the streamer deflects away from its original equilibrium position. The consequent restoring motion may excite the wavelike oscillations propagating along the plasma sheet. Therefore, the geometry supporting the discussed streamer wave motion can be simplified as a long slender plasma slab extending to infinity with the lower end attaching to the streamer cusp which bounces back and forth in a quasi-periodic manner. The oscillations are observed to be generally transverse to the nominal direction of the magnetic field. The manifestation and the geometry of the phenomena are very similar to that of the well-known kink mode deduced from a slender magnetic slab except being in a spherical expanding geometry (Roberts 1981; Edwin & Roberts 1982). It is therefore suggested that the wave phenomenon discussed in this study represents the kink mode, which is, in a more general sense, a type of fast magnetosonic wave propagating in an inhomogeneous magnetized plasma environment. It is interesting to note that the morphology of the streamer wave discussed above is very similar to a traditional Chinese dance

named the "Colored Belt Dance" which is performed by dancers holding one end of a long belt in color.

An important extension to the coronal wave study is to develop diagnostic techniques of plasmas and magnetic fields through which the wave propagates, i.e., to conduct the study of coronal seismology. In our case, the period and phase speed of the streamer wave which has been regarded as the propagating kink mode carried by the thin plasma sheet, if well resolved from observations, can be used to provide information on magnetic properties of streamers. Generally speaking, the phase speed for the wave phenomenon investigated in this study is given by the sum of two components. The first one is the speed of the solar wind along the plasma sheet, the medium carrying the mode outward. The other is of course the phase speed of the wave mode in the plasma rest frame. The phase speed for the kink mode under thin plasma sheet geometry can be tentatively described with available MHD theory developed for a plasma-slab configuration in Cartesian geometry (Roberts 1981; Edwin & Roberts 1982). Substituting nominal parameters in the slow-wind plasma sheet region above the streamer cusp into the dispersion relation given by Edwin & Roberts (1982), we find that the phase speed of the relevant fast kink body mode c_k is smaller than yet rather close to the external Alfvén speed $v_{Ae} = B_e/\sqrt{\mu_0 n m_p}$, where n is the proton number density and m_p the proton mass. The difference between the deduced c_k and v_{Ae} is generally less than one-third of v_{Ae}. Therefore, to implement a preliminary seismological study on the magnetic field strength B_e, we take v_{Ae} to be equal to the kink mode phase speed c_k estimated from our observations.

Regarding the solar wind conditions in the concerned region, the readers are referred to relevant observational studies (Sheeley et al. 1997; Wang et al. 2000; Strachan et al. 2002; Song et al. 2009) and theoretical modelings (e.g., Wang et al. 1998; Suess et al. 1999; Chen & Hu 2001, 2002; Hu et al. 2003; Li et al. 2006). In this short discussion, we simply make use of the solar wind conditions obtained by Chen & Hu (2001). Only two distances are considered: (1) at 5 $R_\odot$, the solar wind velocity $v_{sw} = 100$ km s^{-1} and $n = 1 \times 10^5$ cm^{-3} and (2) at 10 $R_\odot$, $v_{sw} = 200$ km s^{-1} and $n = 2 \times 10^4$ cm^{-3}. With these assumptions, it is straightforward to deduce c_k and thus v_{Ae} at the plasma rest frame, and then calculate the value of the magnetic field strength B_e at the above two distances in the region surrounding the plasma sheet. Here, we only present our calculations of B_e with the measurements associated with the second phase point P2, whose speeds are 410 km s^{-1} at 5$R_\odot$ and 360 km s^{-1} at 10 $R_\odot$, as read from Figure 5. It is found that the magnetic field strength declines from 0.045 G at 5 $R_\odot$ to 0.01 G at 10 $R_\odot$, indicating a slightly super-radial expansion of the magnetic flux tube from 5 to 10 $R_\odot$. These values are consistent with the results given by recent corona and solar wind models (e.g., Li et al. 2006). A more complete seismological study, together with sophisticated numerical MHD simulations of CME–streamer interactions to shed more light on the excitation and propagation of the waves, should be conducted in future.

The SOHO/LASCO data used here are produced by a consortium of the Naval Research Laboratory (USA), Max-Planck-Institut für Aeronomie (Germany), Laboratoire d'Astronomie Spatiale (France), and the University of Birmingham (UK). The CME catalog employed in our study is generated and maintained at the CDAW Data Center by NASA and The Catholic University of America in cooperation with the Naval Research Laboratory. SOHO is a project of international cooperation between ESA and NASA. This work was supported by grants NNSFC 40774094, 40825014, 40890162, 40904047, NSBRSF G2006CB806304, and a Foundation for the Author of National Excellent Doctoral Dissertation of People's Republic of China (2007B24). We thank Kai Liu and Chenglong Shen for their assistance in data manipulations.

REFERENCES

Aschwanden, M. J. 2004, Physics of the Solar Corona: An Introduction (Chichester, UK: PRAXIS)
Aschwanden, M. J., Fletcher, L., Schrijver, C. J., & Alexander, D. 1999, ApJ, 520, 880
Bemporad, A., Poletto, G., Landini, F., & Romoli, M. 2008, Ann. Geophys., 26, 3017
Bemporad, A., et al. 2005, ApJ, 635, L189
Berghmans, D., & Clette, F. 1999, Solar Phys., 186, 207
Chen, Y., & Hu, Y. Q. 2001, Sol. Phys., 199, 371
Chen, Y., & Hu, Y. Q. 2002, Ap&SS, 282, 447
DeForest, C. E., & Gurman, J. B. 1998, ApJ, 501, L217
Edwin, P. M., & Roberts, B. 1982, Sol. Phys., 76, 239
Howard, R. A., et al. 1985, J. Geophys. Res., 90, 8173
Hu, Y. Q., Habbal, S. R., Chen, Y., & Li, X. 2003, J. Geophys. Res., 108, 1377
Hundhausen, A. J. 1993, J. Geophys. Res., 98, 13177
Hundhausen, A. J., Holzer, T. E., & Low, B. C. 1987, J. Geophys. Res., 92, 11173
Li, B., Li, X., & Labrosse, N. 2006, J. Geophys. Res., 111, A08106
Moreton, G. E., & Ramsey, H. E. 1960, PASP, 72, 357
Nakariakov, V. M., & Verwichte, E. 2005, Living Rev. Solar Phys., 3, http://www.livingreviews.org/lrsp-2005-3
Nakariakov, V. M., et al. 1999, Science, 285, 862
Ofman, L. 2009, Space Sci. Rev., 149, 153
Ofman, L., Nakariakov, V., & DeForest, C. E. 1999, ApJ, 514, 441
Ofman, L., Romoli, M., Poletto, G., Noci, G., & Kohl, J. L. 1997, ApJ, 491, L111
Pneuman, G. W., & Kopp, R. A. 1971, Sol. Phys., 18, 258
Roberts, B. 1981, Sol. Phys., 69, 39
Schatten, K. H., Wilcox, J. M., & Ness, N. F. 1969, Sol. Phys., 6, 442
Sheeley, N. R., Hakala, W. N., & Wang, Y. M. 2000, J. Geophys. Res., 105, 5081
Sheeley, N. R., & Wang, Y. M. 2007, ApJ, 655, 1142
Sheeley, N. R., et al. 1997, ApJ, 484, 472
Sime, D. G., & Hundhausen, A. J. 1987, J. Geophys. Res., 92, 1049
Song, H. Q., Chen, Y., Liu, K., Feng, S. W., & Xia, L. D. 2009, Sol. Phys., 258, 129
Strachan, L., Suleiman, R., Panasyuk, A. V., Biesecker, D. A., & Kohl, J. L. 2002, ApJ, 571, 1008
Suess, S. T., & Nerney, S. F. 2006, Geophys. Res. Lett., 33, L10104
Suess, S. T., Wang, A. H., Wu, S. T., & Nerney, S. F. 1999, Space Sci. Rev., 87, 323
Thompson, B. J., et al. 1998, Geophys. Res. Lett., 25, 2465
Wang, A. H., Wu, S. T., Suess, S. T., & Poletto, G. 1998, J. Geophys. Res., 103, 1913
Wang, Y. M., et al. 2000, J. Geophys. Res., 105, 25133
Wills-Davey, M. J., & Thompson, B. J. 1999, Sol. Phys., 190, 467